LSST Camera focal plane optimization

Yousuke Utsumi, Pierre Antilogus, Pierre Astier, John Banovetz, Andrew Bradshaw, Johan Bregeon, Alex Broughton, James Chiang, Celinn Combet, Guillaume Dargaud, et al.

LSST Camera Focal Plane Optimization

Yousuke Utsumi[1,2], Pierre Antilogus[3], Pierre Astier[3], John Banovetz[4], Andrew K. Bradshaw[1], Johan Bregeon[5], Alex Broughton[6], Jim Chiang[1], Celine Combet[5], Guillaume Dargaud[5], Seth W. Digel[1], Johnny Esteves[7], Thibault Guillemin[8], Tony Johnson[1], Claire Juramy[3], Craig Lage[9], Shuang Liang[1], Stuart Marshall[1], Myriam Migliore[5], Homer Neal[1], Renee Nichols[10], Daniel Polin[9], Andrew P. Rasmussen[1], Steve Ritz[10], Eli Rykoff[1], Aaron Roodman[1], Theo Schutt[1], Adrian Sheshtakov[10], Adam Snyder[9], Gregg Thayer[1], Max Turri[1], Tony Tyson[9], and Duncan Wood[10]

[1]SLAC National Accelerator Laboratory, 2575 Sand Hill Rd., Menlo Park, CA 94025, USA
[2]National Astronomical Observatory of Japan, 2-21-1 Osawa, Mitaka, Tokyo 181-8588, Japan
[3]Laboratoire de Physique Nucléaire et des Hautes Energies, Université Pierre et Marie Curie, Université Paris Diderot, CNRS/IN2P3, 4 place Jussieu, 75005 Paris, France
[4]Brookhaven National Laboratory, Upton, NY 11973, USA
[5]Laboratoire de Physique Subatomique et de Cosmologie, Université Grenoble-Alpes, CNRS/IN2P3, 53 av. des Martyrs, 38026 Grenoble cedex, France
[6]Department of Physics and Astronomy, University of California, 4129 Frederick Reines Hall, Irvine, CA 92697, USA
[7]Department of Physics, University of Michigan, Ann Arbor, MI 48109, USA
[8]Université Grenoble-Alpes, Université Savoie Mont Blanc, CNRS/IN2P3 Laboratoire d'Annecy-le-Vieux de Physique des Particules, 9 Chemin de Bellevue – BP 110, F-74940 Annecy-le-Vieux Cedex, France
[9]Physics Department, University of California, One Shields Avenue, Davis, CA 95616, USA
[10]Santa Cruz Institute for Particle Physics and Physics Department, University of California–Santa Cruz, 1156 High St., Santa Cruz, CA 95064, USA

ABSTRACT

The LSST Camera for the Vera C. Rubin Observatory has been constructed at SLAC National Accelerator Laboratory. The Camera covers a 3.5-degree field of view with 3.2 gigapixels. The goal of the LSST survey is to provide a well-understood astronomical source catalog to the community. The LSST Camera's focal plane is populated by 189 sensors on the science focal plane that are a combination of E2V CCD250 and ITL STA3800 deep-depletion, back-illuminated devices, accompanying eight guide sensors, and four wavefront sensors. Nine science sensors are grouped as a "Raft" with three identical electronics boards (REBs), each operating three sensors. The REB can change the operating voltages and CCD clock, allowing operation of sensors from two different vendors in the same focal plane. We conducted phased electro-optical testing campaigns to characterize and optimize the sensor performance in the construction phase. We collected images with the focal plane illuminated by flat illuminators and some specialty projectors to produce structured images. During these tests, we found some performance issues in noise, bias stability, gain stability, image persistence, and distortion in flat images, including "tearing". To mitigate those non-idealities, we attempted different clocking and operation voltages and switching from unipolar voltages to bipolar voltages in parallel clock rails for E2V devices. We describe the details and the results of the optimizations.

Keywords: Vera C. Rubin Observatory, Wide field imaging, CCD, optimization

Further author information: (Send correspondence to YU)
YU: E-mail: youtsumi@slac.stanford.edu, Telephone: +1 (650) 926-4131

1. INTRODUCTION

The Legacy Survey of Space and Time (LSST) is a planned 10-year, deep optical and near infrared imaging survey, which will be conducted at the Vera C. Rubin Observatory, Chile,[1] with the survey planned to start in 2025. The telescope has three mirror surfaces with a primary mirror aperture of 8.4 m. With a 3-corrector lens system, the camera will realize seeing-limited imaging across a field-of-view of 3.5° in diameter.

To achieve the stringent performance requirements for the LSST camera, the focal plane is instrumented with custom, n-channel charge-coupled devices (CCDs) with 100 μm thickness and 10×10 μm pixel dimensions. Each CCD sensor has approximately 4k×4k pixels, totaling 3.2 Giga-pixels for the entire camera. Each CCD is divided into 16 segments (each ∼500×2000), read out in parallel, to achieve low read noise while the entire array is read out in 2 s. The instrumented focal plane (diameter about 65 cm) has an array of 189 mosaiced CCD imaging sensors, in 21 'science rafts',[2] each hosting a 3 × 3 array of CCDs and their readout electronics (readout electronics board, or REBs). In addition, the focal plane has four 'corner rafts',[3] to be used for guiding and focusing, each of which has two of the full-format CCDs and a pair of half-size sensors, each 2k × 4k, with small offsets above and below the plane defined by the science raft sensors that together form a wavefront sensor.

CCDs of two different designs, fabricated by different vendors to meet the performance specifications derived for LSST CCDs,[4] are incorporated in the focal plane: CCD250 from Teledyne e2v (E2V) and STA-3800C from Imaging Technology Laboratory (ITL). The CCDs are back illuminated, with 100 micron thickness Si, for good sensitivity in the red. The CCDs are operated in fully depleted mode. The image format is slightly different for the two CCD designs, and operating voltages and clocking are different.

Sensors were delivered to Brookhaven National Laboratory, where they were characterized individually and integrated into science rafts, each hosting sensors exclusively of one type, E2V or ITL.[5] The science rafts were delivered to SLAC National Accelerator Laboratory, where they were retested individually and eventually integrated into the SiC grid contained in the LSST Camera cryostat. Corner rafts were assembled at SLAC. We tested individual rafts in a small cryostat with a flat illuminator which has tunable wavelength from 320 nm to 1100 nm. Installation of rafts in the camera cryostat started in early 2020, with intervals of interim electro-optical testing after two and then nine rafts were integrated.

Early characterization and optimization efforts have been made and presented. Ref 6 reported early characterization of the sensors and pointed out persistence for E2V devices. Refs 7, 8 described efforts on improving CTE for ITL devices. Ref 9 presented studies on "tree rings", the "brighter-fatter" effect, and charge transfer inefficiency (CTI). The brighter-fatter effect is a dynamic CCD response to source measurement, which repels charge from the centers of bright sources, creating a flux dependence in the point-spread-function (PSF) width. Ref 10 reported physical and electrical analysis of LSST sensors. Ref 11 characterized the "tree ring" effect, which is imprinted in a CCD sensor while fabrication process. Ref 12 reported the inhomogeneity in flat images called "tearing". Ref 13 studied CCD response to the measurement of artificial stars. Ref 14 studied correction method of Brighter-Fatter Effect.

In this paper we present investigations of the performance characteristics of the LSST Camera CCDs as measured in electro-optical testing at SLAC National Accelerator Laboratory.[15–17] This work also included optimization of sequencer timing and voltages for operating the CCDs to mitigate non-idealities of the sensor performance. Other characteristics of the focal plane array, e.g., the flatness, will be presented elsewhere.

2. LSSTCAM FOCAL PLANE

Refs 2, 18 described in detail how the CCDs and readout electronic boards (REBs) are organized into the Raft Tower Modules (RTMs), or rafts for short. An RTM is a self-contained, fully-testable and serviceable imager, containing nine CCDs for a science raft and three for a corner raft, with a complete readout electronics chain. To minimize noise and cross talk between readout channels, each raft is housed in a compact enclosure fully contained within the camera cryostat.

The cryostat holds the grid that supports the science rafts and corner rafts. The REBs in the rafts are thermally coupled to counter-flowing Cold (nominally −40 C) refrigeration circuits, and each CCD is cooled by the cryo plate which in turn is cooled by six Cryo (nominally −130 C) refrigeration circuits, resulting in CCD

Quantity	**e2V CCD**	**ITL CCD**
Segment pixels (vertical × horizontal)	2002 × 512	2000 × 509
Serial pre-scan pixels	10	3
Serial over-scan pixels	22	32
Parallel over-scan pixels	46	48
Number of parallel phases	4	3

Table 1. Pixel dimensions of the E2V and ITL image segments along with the pre- and overscan pixel counts

Tag	UPD	PA2	CJ1	BP1	Run 3	Run 5
PclkHigh	9.0	3.0	3.3	5.3	3.4	3.3
PclkLow	0.0	−7.0	−7.1	−5.5	−5.8	−6.0
SclkHigh	9.5	4.9	5.0	5.3	4.7	3.9
SclkLow	0.5	−4.0	−4.0	−4.2	−4.2	−5.4
RgHigh	11.7	8.5	6.6	7.8	6.4	6.1
RgLow	1.0	−2.0	−3.5	−2.9	−3.4	−4.0
OG	4.0	−1.5	−1.6	−1.7	−2.2	−3.4
RD	18.0	13.5	12.5	13.3	12.7	11.6
OD	30.0	25.0	24.2	25.1	24.4	23.4
GD	26.0	26.0	26.0	26.0	26.0	26.0
Tearing	yes(c)	no	no	yes(v)	yes(v)	no

Table 2. Voltages (in V) for E2V devices. A simple voltage schematic for the serial register (i.e., defining all of the tags in this table except for GD, PclkHigh, and PclkLow) is displayed in Figure 2 of Ref 7. The Tag row indicates the name of the set of voltages. The Tearing row indicates if tearing is present or not; see Sec. 5.3. (c) means the tearing appears in the form of the classical tearing, while (v) in the form of the divisadero tearing.

temperatures of −100 C, with active heater control. The rafts are organized in a grid of 5×5 bays, with a corner raft at each corner and science rafts in the other bays.

The top left figure in Figure 3 is a map of the focal plane. The rafts are designated according to their x-y location, e.g., R00 for the lower left and R22 for the center. They are also labeled with raft identifiers with RTM or Corner Raft Tower Module (CRTM) numbers. The rafts are color coded according to manufacturer of their CCDs: E2V science rafts are gold, ITL science rafts are green, and the corner rafts (also ITL) are cyan. The individual sensors in each science raft are designated S00, S01, etc. according to their locations. The corner rafts have SW0 and SW1 designators for the wavefront sensors and SG0 and SG1 for the guide sensors. The subdivision of each CCD into image segments, which are read out in parallel, is also indicated.

2.1 Raft electronics and the data acquisition system

Each REB controls two types of voltages: bias and clock. Bias voltages are fixed voltages to be supplied to a CCD (Output Gate: OG; Reset Drain: RD; Output Drain: OD; Guard Drain: GD), while clock rail voltages are the voltages for high and low states provided to an electrode to drive a CCD.(Parallel Clock: Pclk; Serial Clock: Sclk; and Reset Gate: RG). Each REB has an FPGA whose firmware configures the board components, such as an ASIC for signal processing (Analog Signal Processing Integrated Circuit; ASPIC), defines the timing states and sequences, serializes and transmits the 18-bit data, and communicates with the host via a custom protocol having virtual channel capability.[2,19,20] This flexibility provides the ability to operate either kind of CCD, with type-specific voltages, in units of 3 sensors individually.

2.2 Focal Plane Charge-Coupled Devices and their voltages

Table 1 describes the sensor formats for both vendors. The numbers are quite similar but they are different in the details. The number of parallel phases is also different.

Tables 2 and 3 list the combinations of configuration voltages for E2V and ITL that we explored during the focal plane testing period. The 'Tag' designators in the column headings are internal shorthand for a given set of voltages. The primary purposes for testing out these sets of voltages were overcoming the tearing issue for E2V sensors and stabilizing gain for ITL sensors. These are discussed in Sec. 5.3.

Tag	Run 3	Run 5
PclkHigh	2.0	2.0
PclkLow	−8.0	−8.0
SclkHigh	5.0	5.0
SclkLow	−5.0	−5.0
RgHigh	8.0	8.0
RgLow	−2.0	−2.0
OG	−2.0	−2.0
RD	13.0	13.0
OD	25.0	26.9
GD	20.0	20.0

Table 3. Same as Table 2 but for ITL

The initial recommended set of operation voltages from the vendor were unipolar. The unipolar configuration is to have both parallel rail voltages positive. However, we have switched from the unipolar voltages to bipolar voltages for which the parallel high voltage is positive and the parallel low voltage is negative as recommended in Ref 12 as an effort to mitigate the tearing effect in E2V CCDs (see Section 5.3).

Since the voltage optimization is an optimization in a high dimensional parameter space, not all of which is safe for operating the CCDs, we explored configurations that obeyed the following relations, allowing only slight deviations from these rules. This constraint is only used for E2V devices. Given PclkLow, PclkSwing, SclkSwing, RgSwing, ΔRD

$$\begin{aligned}
\text{PclkHigh} &= \text{PclkLow} + \text{PclkSwing} && (1)\\
\text{RD} &= \text{PclkHigh} + \Delta\text{RD} && (2)\\
\text{OD} &= \text{RD} + 11.8 && (3)\\
\text{OG} &= \text{RD} - 15.0 && (4)\\
\text{SclkLow} &= \text{OG} - 2.0 && (5)\\
\text{SclkHigh} &= \text{SclkLow} + \text{SclkSwing} && (6)\\
\text{RgHigh} &= \text{RD} - 5.5 && (7)\\
\text{RgLow} &= \text{RgHigh} - \text{RgSwing} && (8)\\
\text{GD} &= 26 && (9)
\end{aligned}$$

This rule was constructed for making sure amplifiers functioning correctly, according to the choice of high and low rail voltages or a difference high and low rail voltages (swing).

2.3 Sequencer

The clock timing is defined in an ASCII formatted "sequencer file". The current up-to-date sequencer files based on the optimization work we have done are: `FP_E2V_2s_ir2_v26.seq` and `FP_ITL_2s_ir2_v26.seq` for E2V and ITL sensors, respectively, which are publicly available*.

The nominal CCD operation for an image acquisition follows: clear (ClearCCD), integration (Integrate), and readout (Read), where the word in parenthesis corresponds to the top level blocks of operation called "mains" defined in the sequencer file. ClearCCD performs two full parallel transfers and inverts the parallel clocks for a given time. While in the Integrate state, we run serial register continuously to flush charges in the serial register for ITL CCDs and just toggle CL slowly for E2V sensors for avoiding the glow from the serial register. CL is the ASPIC clamp which is a switch to restore the DC level of the input signal to the input reference to ASPIC. Read has a more complicated operation. Figure 1 shows a scan mode output for a pixel read. The scan mode output displays how the sequencer states were set as well as signal output from a CCD before and after integration in the correlated double sampling readout. The timings are defined by parameters such as BufferS, ISO1, RampTime, BufferS, ISO2. The integration occurs at RampTime.

*See https://github.com/lsst-camera-dh/sequencer-files/blob/master/run6/

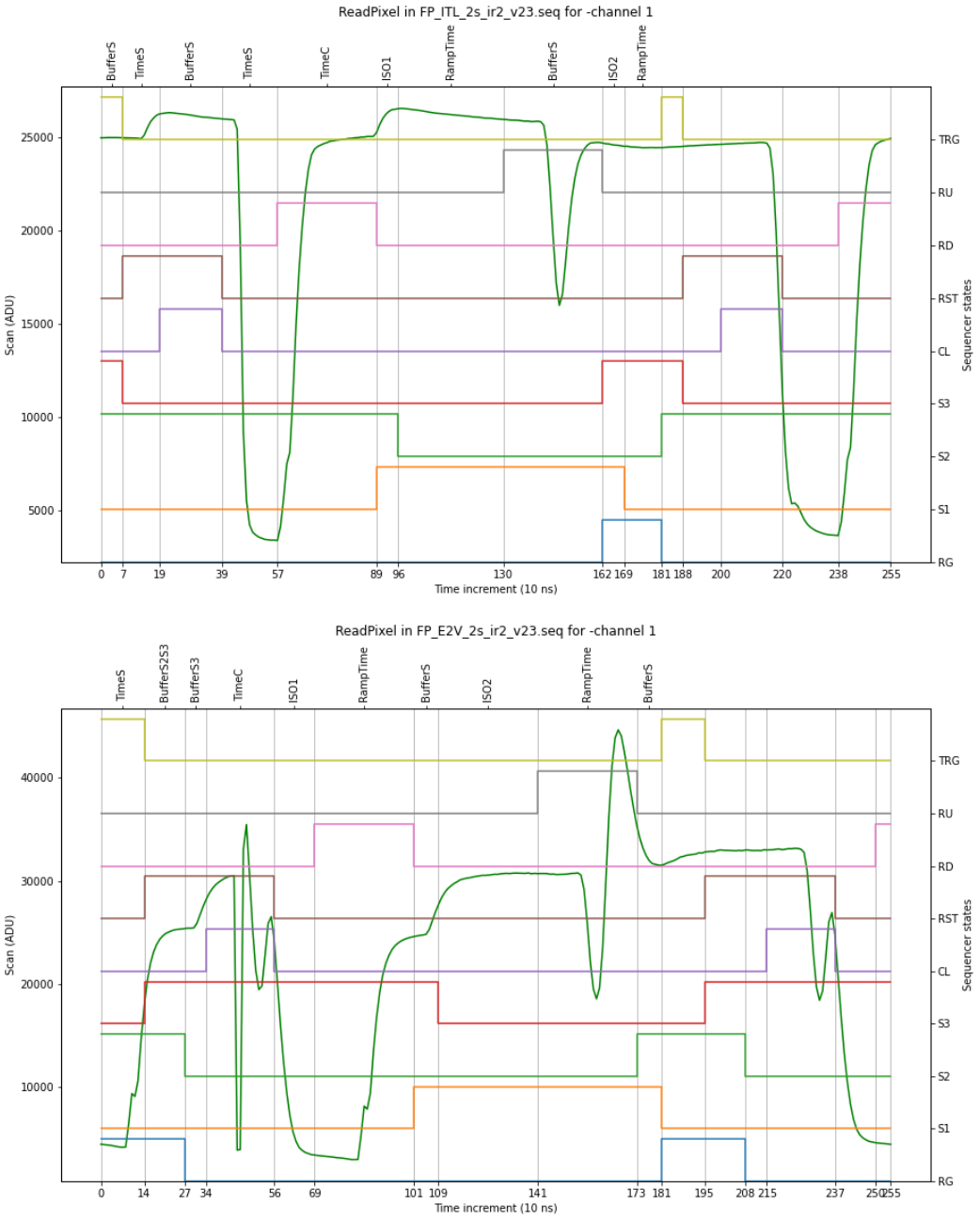

Figure 1. An analog voltage signal output for a single pixel of the CCD for a bias exposure, along with sequencer time profiles for an ITL (top) and E2V (bottom) sensors. The sequencer timings determine the CCD clock. This data was taken with earlier version of sequencer file (v23).

The state between exposures, i.e, when no image is being acquired, can also be configured in the REBs, e.g., in terms of flushing the serial registers. We explored the possibility to improve the bias stability for particular problematic amplifiers discussed in Sec. 6.1 by adjusting the idle state configuration.

2.4 Bench for Optical Testing

The Bench for Optical Testing (BOT)[21] is a high-stiffness platform to support the camera cryostat and integrated rafts in a vertical orientation with the CCDs facing downward. For electro-optical testing, the area beneath the BOT platform is covered to make a light-tight box. For this testing an optical flat was used as the window to the cryostat. In this dark box different types of projectors (some mounted on an x-y stage) are used to characterize the performance of the CCDs and raft electronics. This bench was used on testing the full array of CCDs in the focal plane.

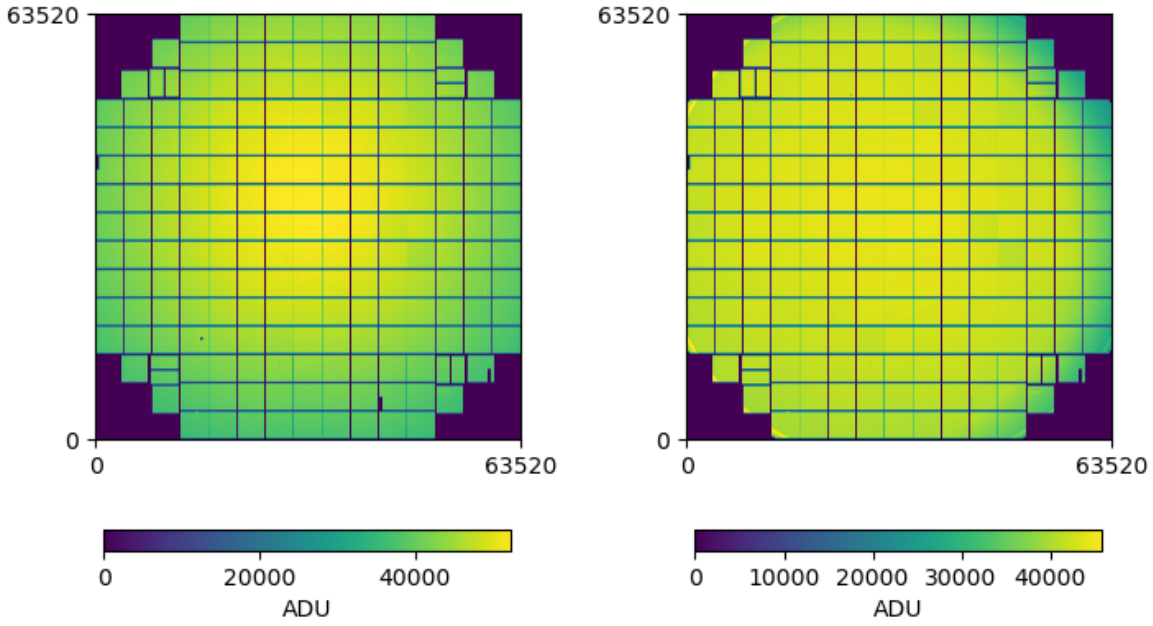

Figure 2. Two examples of flat images taken with the BOT flat projector and the CCOB wide beam projector.

The flat projector has a broadband Xe discharge lamp light source coupled to a shutter and two filter wheels in series. One wheel has a set of SDSS filters (u, g, r, i, z, and Y) and five narrow-band filters and the other has a range of aperture sizes to reduce the intensity of the illumination. The filtered light is coupled to an integrating sphere, the output port of which is re-imaged on the focal plane by a 25 mm f/2.8 lens. The illumination pattern is smoothly varying (Fig. 2), with only small gradients across any CCD image segment. A port on the integrating sphere is also used to illuminate an NIST-calibrated photodiode read out by a Keysight model B2981B picoammeter at 60 Hz. The integrated photodiode current measured in this way is used for quantum efficiency and linearity studies as described in Sec. 3.4.2.

The cross talk spot projector projects a spot on four of the 16 amplifier segments of a CCD at the same time. The projector is oriented so that the spots are in different locations of the four segments so that the spots and their cross talk responses do not coincide with each other in the other amplifiers.

The spot projector provides realistically sized star-like sources on the focal plane. The spot grid projector uses a Nikon 105 mm f/2.8 Al-s Micro-Nikkor lens to re-image the 1" exit port of an integrating sphere that has been masked with the desired optical pattern using an HTA Photomask photo-lithographic mask. The projector has a six-position Thorlabs motorized filter wheel is used to remotely select from a set of masks with various patterns and position the desired mask in front of the integrating sphere exit port. A grid of 49×49 spots, and a thin slit to simulate satellite streaks were extensively used during the testing program. The spot grid projector shares the same 450 nm light emitting diode light source as the cross talk projector and is also equipped with a Thorlabs 1" single-blade optical beam shutter. Details of the spot projector, cross talk projector, and flat illuminator are presented by Ref 17.

LED vendor and part number	$\langle\lambda\rangle$ [nm]	$\Delta\lambda$ (FWHM) [nm]	Corresponding filter name
Seoul Optodevice UV CUN6AF1A	365	12 @ 500 mA	u
OSRAM - LBW5SM	466.6	25 @ 350 mA	g
OSRAM - LAW5SM	622.6	18 @ 400 mA	r
Roithner - APG2C1-760	759.9	28 @ 350 mA	i
Roithner - APG2C1-850	845.7	32 @ 350 mA	z
Roithner - APG2C1-940	950.5	60 @ 350 A	Y

Table 4. LEDs used in the Camera Calibration Optical Bench wide beam projector.

Eight ^{55}Fe soft X-ray sources, each initially 80 μCurie, are mounted inside a flange between the optical flat (cryostat entrance window) and the cryostat. Each source is behind a shutter that when open allows the CCDs in the focal plane to be illuminated obliquely with characteristic 5.9 keV and 6.4 keV X-rays from electron-capture radioactive decay of the ^{55}Fe. These approximately mono-energetic photons free a known number of electron-hole pairs on absorption by a CCD and so can be used to measure the electronic gain (expressed as electrons per ADU of digital readout) for each image segment. The ^{55}Fe ring is installed only for gain measurements with the BOT.

2.5 Camera Calibration Optical Bench

After we assemble the cryostat with the focal plane, the optics, the shutter, the filter exchange system, and the utility trunk, the Camera is placed on what is called the Camera Calibration Optical Bench (CCOB). In this configuration, we can test the whole Camera system as a unit.

We have two projectors for testing the integrated Camera. One is meant to produce a uniform illumination on the focal plane (CCOB Wide beam). The light produced by one of six different LEDs which are controlled by a custom-made LED driver is fed into an integrating sphere and then projected onto the focal plane by a lens. Characteristics of the LEDs are shown in Table 4. An example flat image is displayed in Figure 2. An effort to make the illumination more uniform than the BOT flat projector has been done. A slight off center of the beam can be seen as gradient in the right edge.

The other projector (CCOB Narrow beam) is a single-beam projector coupled with a tunable laser source placed on X/Y and θ/ϕ drives so that throughput of the Camera system can be measured at any given location and angle. We can measure the total throughput by synthesizing beams sampled at different angles and positions. This projector also supports studies of internal reflections and the resulting 'ghost' images.

3. ELECTRO-OPTICAL TEST IMAGE ACQUISITIONS

The results presented here are derived from two periods: data taken with the fully populated LSST Camera focal plane on the BOT during the period 4 November 2021 to 23 February 2022 (called Run 5), and data taken with the fully assembled Camera on the CCOB during the period from June and October 2023 (Run 6). Here we describe the types of images acquired for electro-optical testing during these runs.

During part Run 5 the refrigeration system for cooling the REBs experienced persistent instability. In the results presented here, we exclude data taken during periods of particular variability of the temperatures of the raft electronics. The Cryo refrigeration system for cooling the CCDs worked stably throughout both Run 5 and Run 6.

3.1 Bias frames

These are zero exposure-time images after one ClearCCD that are used to measure the bias (offset from zero ADU) level of the analog-to-digital conversion. These images do have some structure. With the assumption that the structure is stable with time, a series of bias frames is typically medianed together to construct a 'superbias' frame that can be subtracted from other image acquisitions without significant effect on the overall noise level. Note that the assumption of static bias was not found to hold for all sensors; see Sec. 6.1.

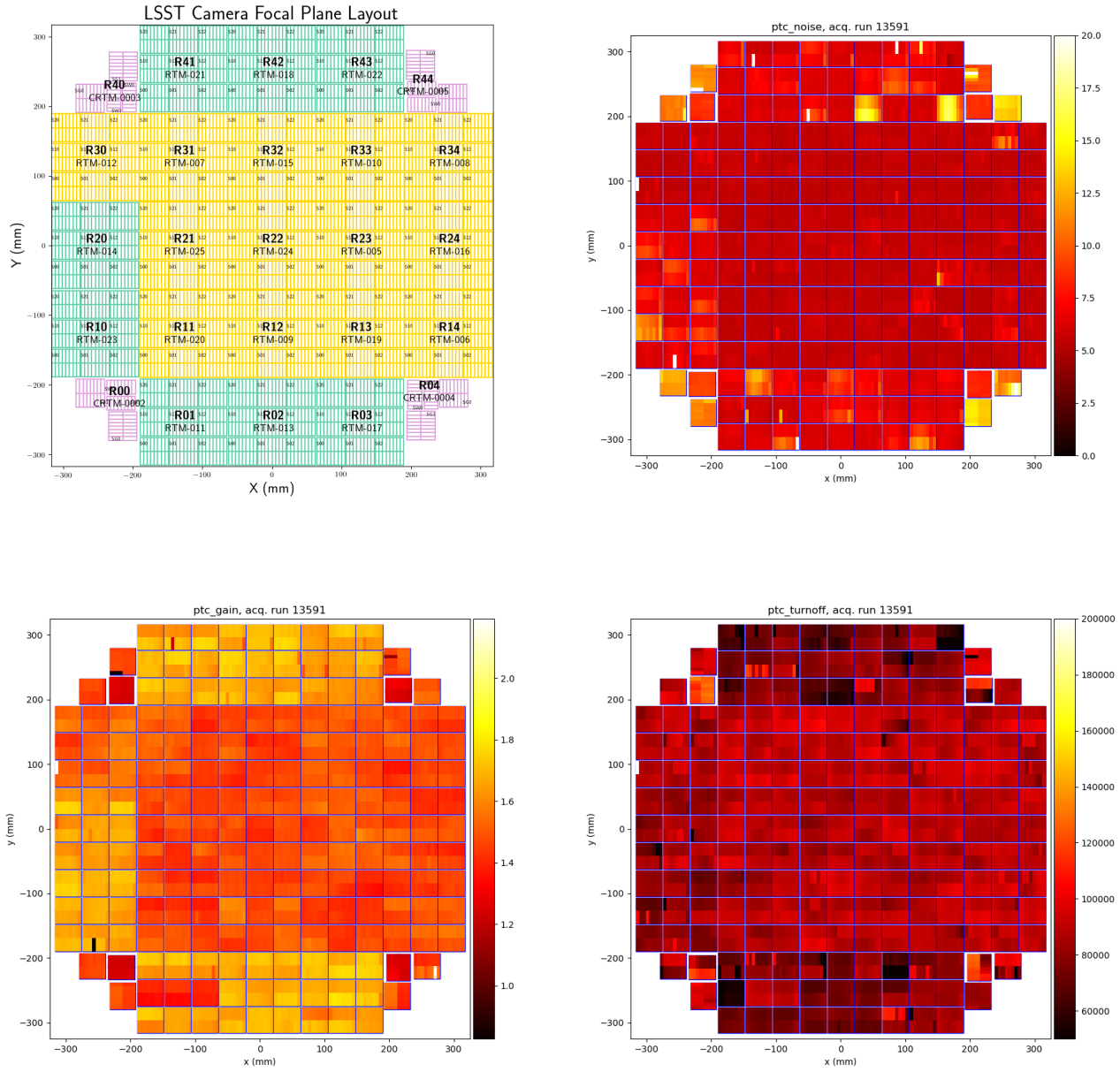

Figure 3. Summary of sensor arrangement in the focal plane along with maps of some basic performance characteristics. (top left) the focal plane layout. (top right) PTC noise (bottom left) PTC gain (bottom right) ptc turnoff

3.2 Dark frames

These are image acquisitions after integration with no illumination on the CCDs. These are used to measure the dark current of the CCDs. Care was taken to eliminate light 'leaks' into the dark box down to 0.05 e-/pixel/sec or below, so that the signal in image acquisitions would be dominated by CCD dark current.

3.3 ^{55}Fe

These are effectively dark frames taken with the shutters open for the ^{55}Fe sources, to expose the CCDs to soft X-rays. Typical exposure times were 15 min and as already noted, these images are used to measure the electronic gain of the CCD readouts.

3.4 Flat images

These are a series of image acquisitions with the CCDs illuminated by the flat projector. These were typically taken wih the r filter. In order to explore full dynamic range of the CCDs, we need to change the amount of the light in addition to exposure time control. We used different aperture filter or different current for the LED light source with exposure time to produce images with a wide range of electrons per pixel (which we will refer to as flux), from $\sim$100 to full well, $\sim 2 \times 10^5$. For each combination of illumination level and exposure time used, a pair of flat images is acquired and these images are used to evaluate gain (through the photon transfer curve method; see Ref 14) and linearity of the electronics. For the results considered here, the acquisitions were in random order by flux, to factor any temporal dependence of performance from flux dependence. During the exposures for flat image acquisitions, the time history of the current through the monitoring photodiode current is recorded by the picoammeter for use as a proportionate measure of illumination.

3.4.1 Flat images – stability

These are sequences of flat image acquisitions at the same flux. These sequences are used to evaluate gain stability over time. As discussed in Sec. 5.7, variations of gain can be correlated with temperature variations of the REBs.

3.4.2 Flat images – wavelengths

These are sequences of flat image acquisitions by different filters. This acquisition was primarily used to measure averaged quantum efficiency over the band paths. However, we used flat images taken at different wavelengths to study structures in flat images. The surface effect is present in bluer wavelengths. This is likely caused by the process to activate silicon lattice after the thinning process to get thinned to 100 μm is applied. ITL appears to use chemical etching whereas E2V uses laser annealing.[13]

3.5 Spot cross talk images & Spot images

In addition to images with uniform flat illuminator, we acquired images with specialized illuminators to project structured illumination onto the focal plane for a selected sensor to study the sensors in detail.

Using the cross talk images the preliminary analysis result is presented in Ref 17 and further detailed analysis will presented in elsewhere.

The spot images are used to study the systematic effect on the measurements of the static sensor anomalies such as tree-ring and surface finish is discussed in Ref 13 and Brighter-Fatter effect.[14]

4. IMAGE REDUCTION AND ELECTRO-OPTICAL PERFORMANCE

We used automated software to characterize electro-optical performance from the test images. The original implementation was presented in Ref 6 and was converted to python and named eotest[†]. In the full camera testing phase, we switched to analysis systems cpPipe[‡] and eoPipe[§] based on the LSST Science Pipelines.[22] Their outputs were compared and confirmed to be consistent.

Using this software, we measured different metrics: read noise, dark current, full well capacity, non-linearity, serial and parallel charge transfer inefficiency, quantum efficiency, pixel response non-uniformity, gain, and point-spread function.

[†] https://github.com/lsst-camera-dh/eotest
[‡] https://github.com/lsst/cp_pipe
[§] https://github.com/lsst-camera-dh/eo_pipe

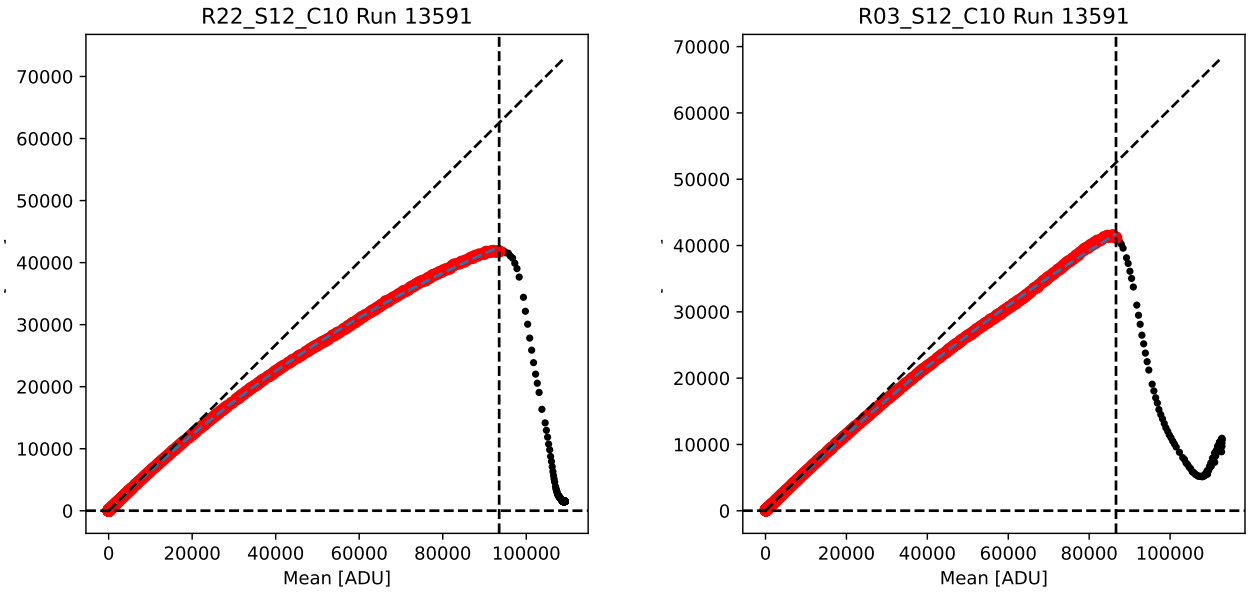

Figure 4. PTC curves, i.e., plots of image variance (ADU^2) vs. image mean for one image segment of 16 of an E2V (left) and ITL (right) sensor. The dots are data points. The fitted data points are colored by red. The dotted curve shows the best fit model. The horizontal, the vertical, and the slope lines correspond to the parameter of the model: the noise level, the PTC turn off, and the gain slope. The deviation from the straight line is the contribution from the Brighter-Fatter effect.

As an example, we show PTC curves for different vendors in Figure 4. The PTC was sampled for about 400 different fluxes to study detailed structure of the sensor response, which provides information on basic sensor performance such as read noise, gain and full well capacity and additionally provides information about the Brighter-Fatter effect from the fitting. The detail model is presented in 14. Figure 3 displays summary plots of read noise, gain, and turnover determined from the PTC fitting for all the sensors. We characterized the 3216 channels. All the plots are publicly available[¶]. Figure 5 shows the distributions of fractional differences of electronic gain measured from the ^{55}Fe and PTC flat pair images, separately for the E2V and ITL science rafts. We confirmed that ^{55}Fe and PTC-determined gains are consistent at the 0.3% level. The origin of the slight bias is uncertain but could be related to the PTC fitting having taken into account only nearest-neighbor pixel covariances.

5. MITIGATION OF NON-IDEAL SENSOR EFFECTS

Here we describe CCD performance issues identified in the electro-optical testing data and the optimizations undertaken to mitigate them.

5.1 Dipoles in ITL devices

In the early phase of our testing, we discovered that flat images taken by ITL sensors exhibited correlated noise along the parallel transfer direction (Figure 7). We call this effect "dipoles" since we observed pairs of pixels that have ~ 10 ADU positive and negative deviation from average, regardless of flux level. The dipoles did not change location from exposure to exposure. We defined a metric for the strength of the dipole effect by comparing covariances between (i, j) and $(i, j+1)$ pixels. The left-hand grid of plots in Figure 7 shows the covariance when a dipole signal is present. The strong correlation across all the amplifiers in one sensor is evident. The right-hand group of plots in Figure 7 shows the result after we implemented the mitigation that changes the number of

[¶]See https://s3df.slac.stanford.edu/data/rubin/lsstcam/13591/w_2023_41/

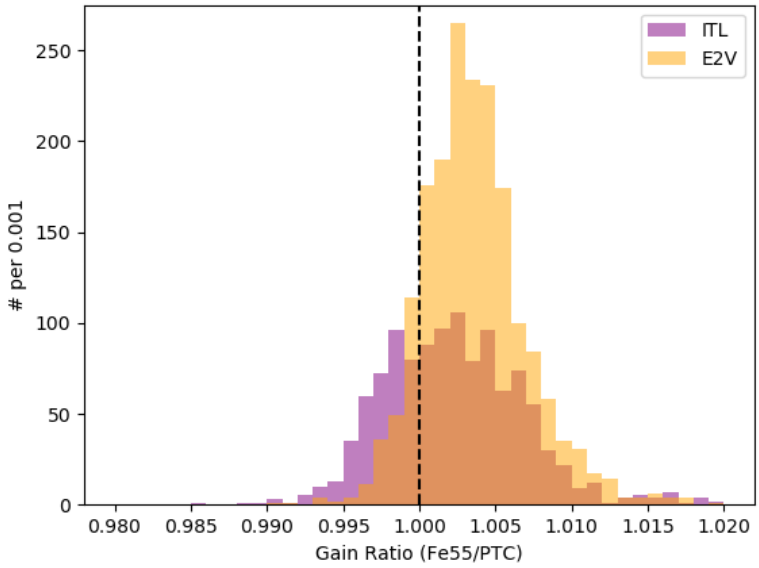

Figure 5. Distributions of gain ratios measured via ^{55}Fe and PTC flat pair images for individual amplifier segments of the E2V and ITL science rafts. The origin of the slight bias is uncertain but could be related to the PTC fitting.

parallel phases held high during integration from 1 to 2. This provided the additional benefit of increasing the full well capacity by $\sim 15\%$.

The interpretation of the dipole effect is that it is due to charge pockets between electrodes of parallel low phases. When integration ends and parallel transfer starts, charges trapped by a pocket between two phases would be divided among two adjacent pixels. This explains the good repeatability.

5.2 Read noise

We adjusted the readout timing parameters to optimize the CCD read noise. Figure 1 shows a timing diagram of a pixel read operation, which includes states of voltages we apply to CCDs and the ADCs as well as the video output signal from the CCD. The timing can be changed in many ways. However, we focus on effects of "RampTime", "ISO1", and "ISO2". RampTime is the integration time for the correlated double sampling (CDS) circuit. Since we measure the signal level twice for the actual signal and the baseline, the pixel read has two time periods of RampTime. ISO1 specifies the waiting time between when it resets the signal and it starts the measurement. ISO2 is the waiting time for charges to settle before measurement. We changed one parameter at a time, and measured readout noise from the overscan regions of bias images collected.

Figures 8, 9, 10 show the result of the readout timing study. The legend has the acquisition numbers and text describing what we changed. The format is expressed in the form of a regular expression, (RT|ISO1|ISO2)[pm](\n*)pct, where RT means RampTime, p or m are + or -, and pct means percent. The results are organized in three groups: E2V Science Rafts, ITL Science Rafts, and ITL Corner Rafts. (The LSST Camera does not have E2V Corner Rafts.) Each group has 4 read noise measurements as functions of total readout time, RampTime, ISO1, and ISO2.

The plots show important results. Read noise decreases as RampTime is increased for both E2V and ITL science sensors, but reaches a plateau for corner raft ITL sensors. The decreasing trend follows the inverse square root of RampTime, which indicates that the read noise is dominated by the CDS integration. Changing ISO1 has little impact on the read noise for both E2V and ITL science sensors. Corner raft ITL sensors respond differently: increasing ISO1 reduces the read noise slightly but not much. Changing ISO2 has little impact on

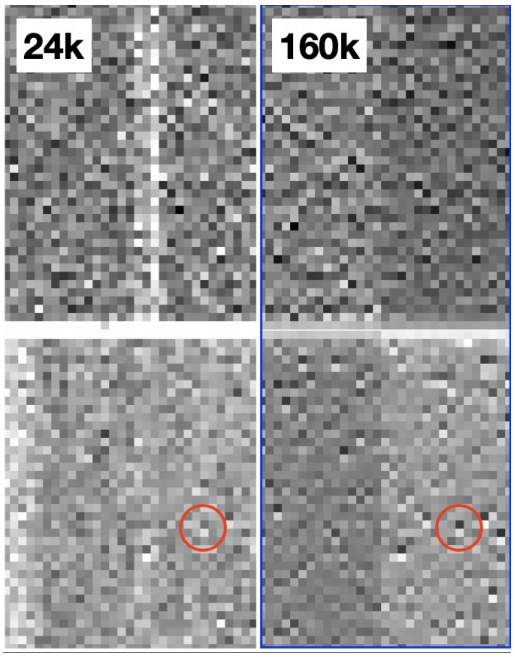

Figure 6. Visual presentation of the dipoles in small sections of flat images at different flux levels at 24k (almost no signal) and 160k (high flux) in the red circles, there is a pair of pixel have negative (black) and positive (white) numbers with respect to the average (grey). The dipoles can be seen everywhere not only in the circle.

the read noise for E2V sensors, while increasing ISO2 slightly decreases the read noise for outliers among the ITL science sensors.

We selected RTp20pct, which increases RampTime by 20% from the nominal sequencer file to reduce the read noise for both E2V and ITL sensors in the science rafts but not to increase it too much for corner rafts, as the overall best.

5.3 Tearing

Continuous, narrow, jagged features (which we have designated 'tearing') seen in flat field images are a visually striking obstacle to performing Pixel Response Non-Uniformity corrections. These patterns can be explained as being due to lateral field distortions, caused by the nonuniform distribution of holes in the channel stops between sensor columns.[12] Originally, we operated the E2V sensors with unipolar voltages, i.e., with all voltages positive except for the Back-Substrate (BSS) bias voltage, which is applied to the back of the sensor to make it fully depleted. A number of efforts were made,[12] with the conclusion that the effect could be largely mitigated by operating the E2V CCDs with bipolar voltage settings, for which lower clock rails have negative voltage and upper clock rails have positive voltage. Early testing confirmed that most tearing is mitigated with bipolar operating voltages (Table 2). However, because the strength of tearing depended on the the sensor, tearing features remained for some CCDs.

Tearing usually manifests in two ways. One kind appears around the midline break ('classical tearing'). The other appears near amplifier boundaries ('rabbit ears' or 'divisadero tearing') (see Figure 11). We also observe, under rare circumstances, a mix of both types. With all CCDs operated with bipolar settings, we explored further mitigations in several ways:

1. Changing the clear operation, which is the clocking to purge charges before the integration clocking. In the clear clocking, we add an inversion by making all parallel clocks low for a certain amount of time to neutralize the hole population.

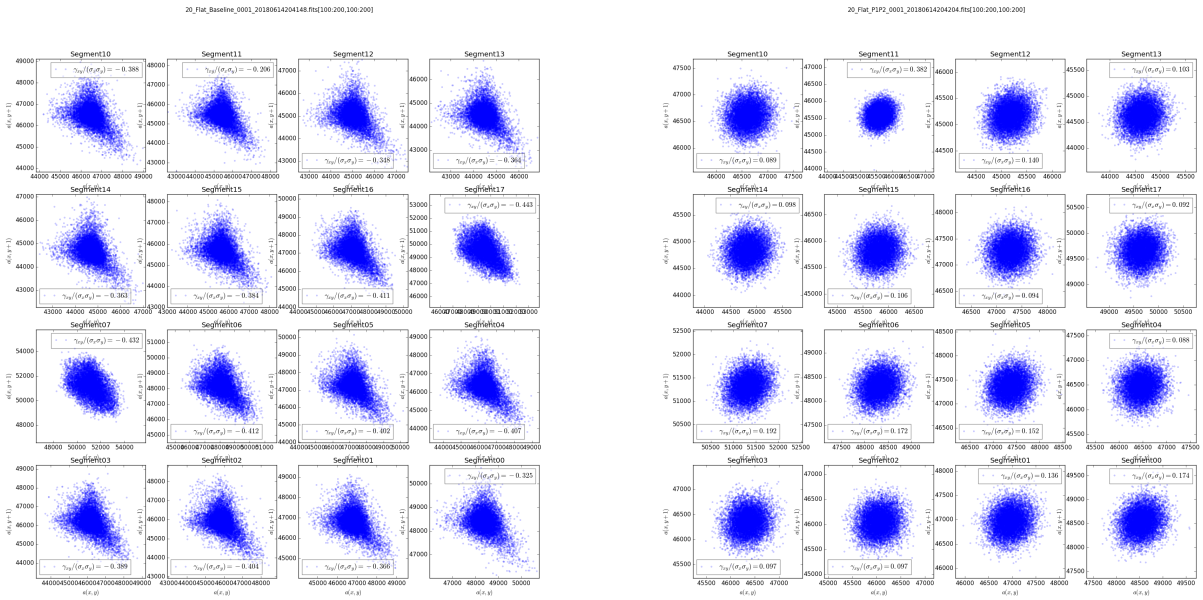

Figure 7. Pixel correlation of 1 pixel lag along the direction of parallel transfer ($\sigma(i, j+1)$ vs. $\sigma(i, j)$) showing the effect of the dipoles (left) and the results after mitigation (right)

2. Changing the BSS. As we observed the tearing was weaker with a BSS of $-70\,\mathrm{V}$ although our target operating voltage is $-50\,\mathrm{V}$, we tried to increase the BSS as much as possible.

3. Changing the parallel lower clock rail. As we observed that decreasing parallel clock low lower than $-6\,\mathrm{V}$ reduced the strength of tearing on the Raft-level sensor testing on the bench, we tested them by changing it to $-6.1\mathrm{V}$ and $-6.2\mathrm{V}$.

4. Changing the parallel swing with the parallel low rail held fixed.

By changing the clock inversion time in the clear clocking, we observed different consequences for the appearance of the divisadero tearing. From our investigation, inverting for 3000 μs works the best to remove the divisadero tearing. The divisadero tearing got worse for either shorter or longer inversion times. We also find making the parallel voltage swing smaller than nominal works to remove the classical tearing. We found a parallel swing of $9.3\,\mathrm{V}$ worked but $9.4\,\mathrm{V}$ did not. All other attempts, such as changing BSS to $-50\,\mathrm{V}$, or changing the parallel lower clock rail, had positive effects on the tearing, but were insufficient to completely remove the effect over the range we explored.

5.4 Long-range serial correlations

Correlation of pixels is observed in their covariances. The strength evolves quadratically as a function of flux. Not all the sensors have this long-range serial correlation. The effect is not homogeneous across a CCD but varies amplifier by amplifier. An initial assessment found only six sensors (each E2V) affected. Previous raft-level testing did not show this effect. This pixel correlation is reproducible if the gain variation from row-by-row is random and of the order of 0.002.

We originally used the following equation to determine the RD voltage.

$$\mathrm{RD} = \mathrm{PClk_{Low}} - 0.8 \times \mathrm{PClk_{Swing}} + 16.72 \tag{10}$$

Switching to the new formula in the following

$$\mathrm{RD} = \mathrm{PClk_{High}} + 8.0 \tag{11}$$

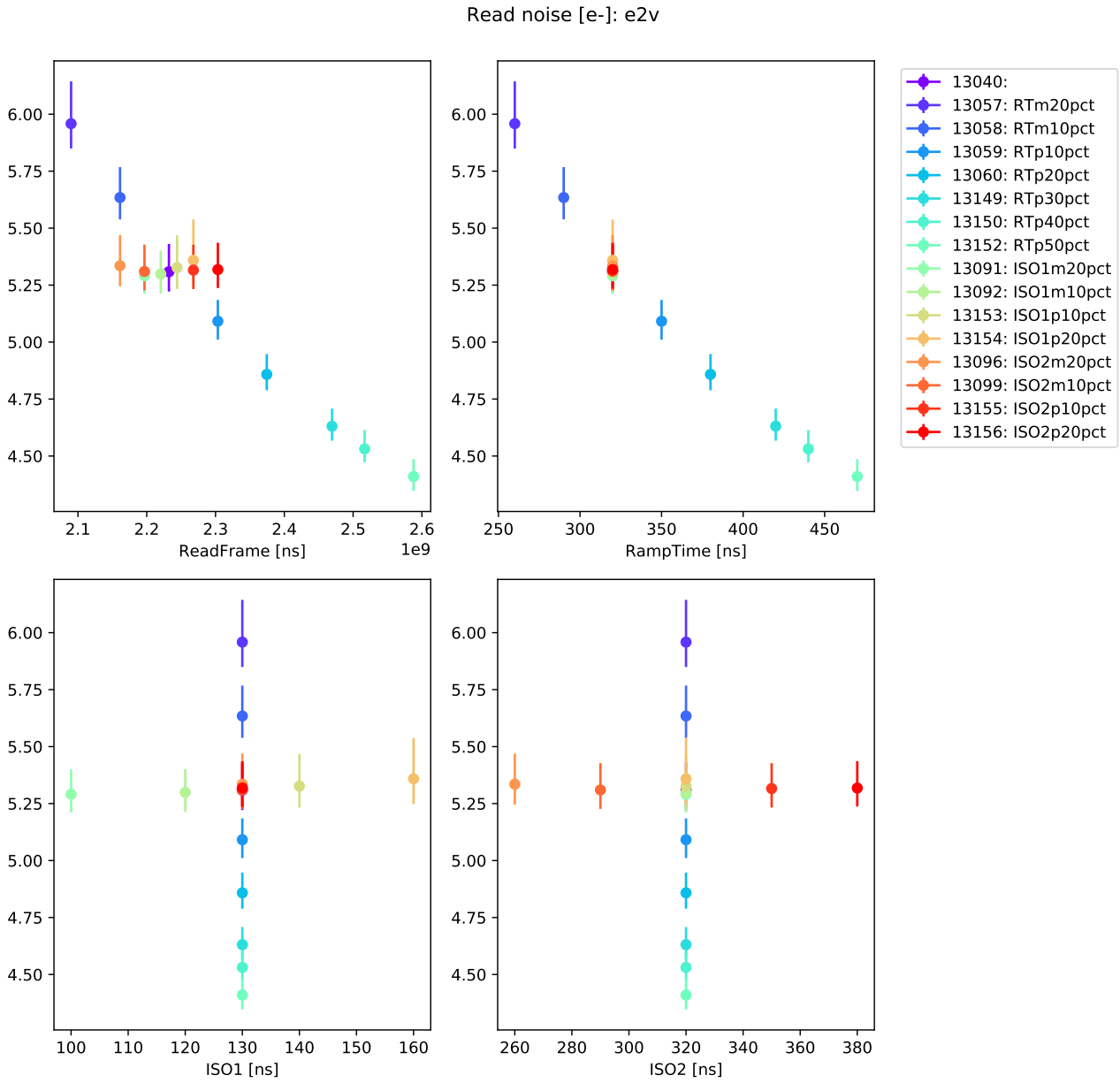

Figure 8. Readout noise in electrons for E2V with different sequencer timings. The symbols are placed at the median (50th percentile) and error bars indicate 1 σ equivalent (32nd and 68th percentiles).

greatly reduced the random gain. This suggests that incomplete reset of the second stage amp was the cause.

5.5 Gain jumps

In order to study the gain stability we acquired a series of flat images over 30 minutes. During the acquisitions we monitored the brightness of the light source using a photodiode. We divided the mean signal in an amplifier by the photodiode signal to assess the stability of the gain. For the initial value of OD (25.0 V), the gains for ITL rafts exhibited discrete jumps of up to 1% from acquisition to acquisition (Figure 12).

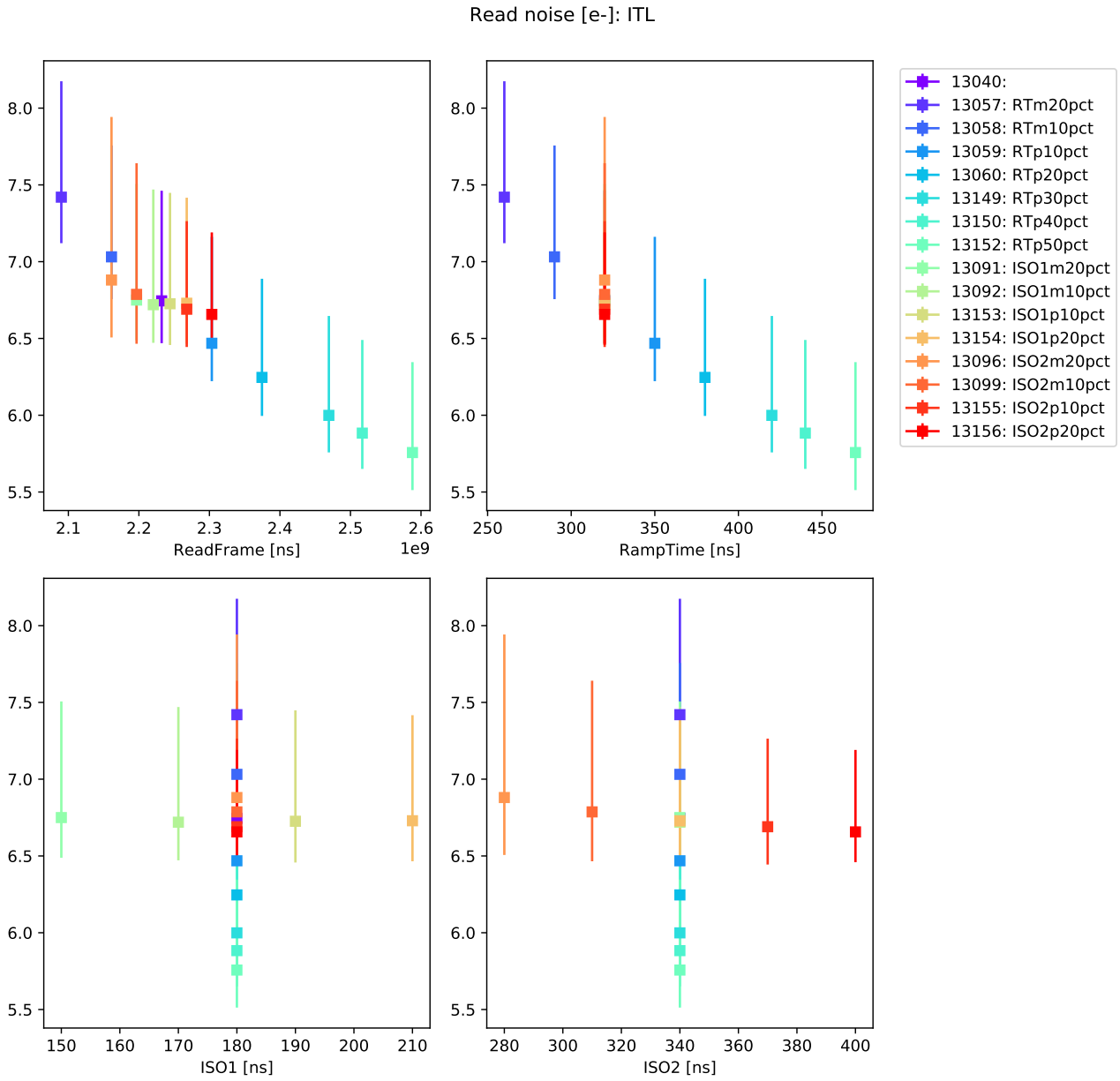

Figure 9. Same as Figure 8 but for the sensors on the ITL Rafts.

We performed acquisitions for a range of OD from 25.0 V to 26.9 V using a spare ITL raft in a test stand. We found that 26.9 V gives good enough gain stability of below 0.1%. Ref 7 made a detailed study of gain change in the OD-RD plane and concluded that the output amplifier behaves stably for OD $>$ 26.5 V. We applied this change to the focal plane operation and we found that adjusting OD to 26.9 V for ITL mitigated this effect nearly entirely.

The OD voltage controls the operation of the output amplifier. Our optimization brought the OD setting nearly back to what was used in early testing Ref 7, 27.0 V.

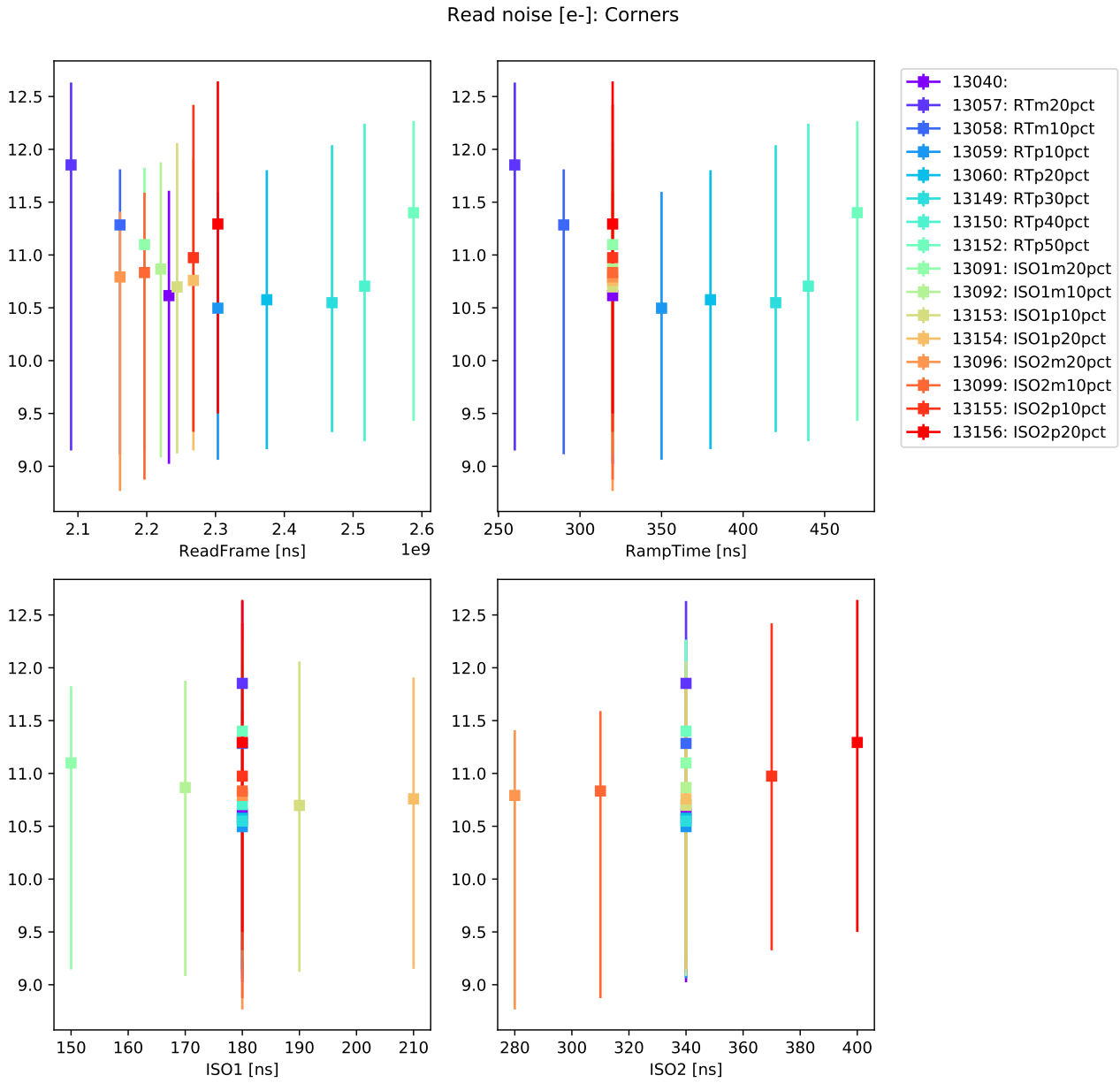

Figure 10. Same as Figure 8 but for the sensors on the corner Rafts

5.6 Full well & parallel timing

In the course of testing, we tweaked the timings for the parallel transfer. In the parallel transfer, the time spent in each phase is defined as TimeP. The initial TimeP was 5000 ns and we scanned the full well by changing TimeP up to 10000 ns, in six steps of 1000 ns between 5000 ns and 10000 ns.

Figure 14 shows the result. The full well capacity grows as TimeP increases but rolls off at 7000 ns. We chose 7000 ns as the optimum setting for TimeP This testing was done with ITL sensors. E2V sensors have slightly more complicated timing. However, the timing needs to be matched with ITL so that they do not interfere with each other. We tweaked E2V timing so that the total time of the parallel transfer matches the ITL parallel

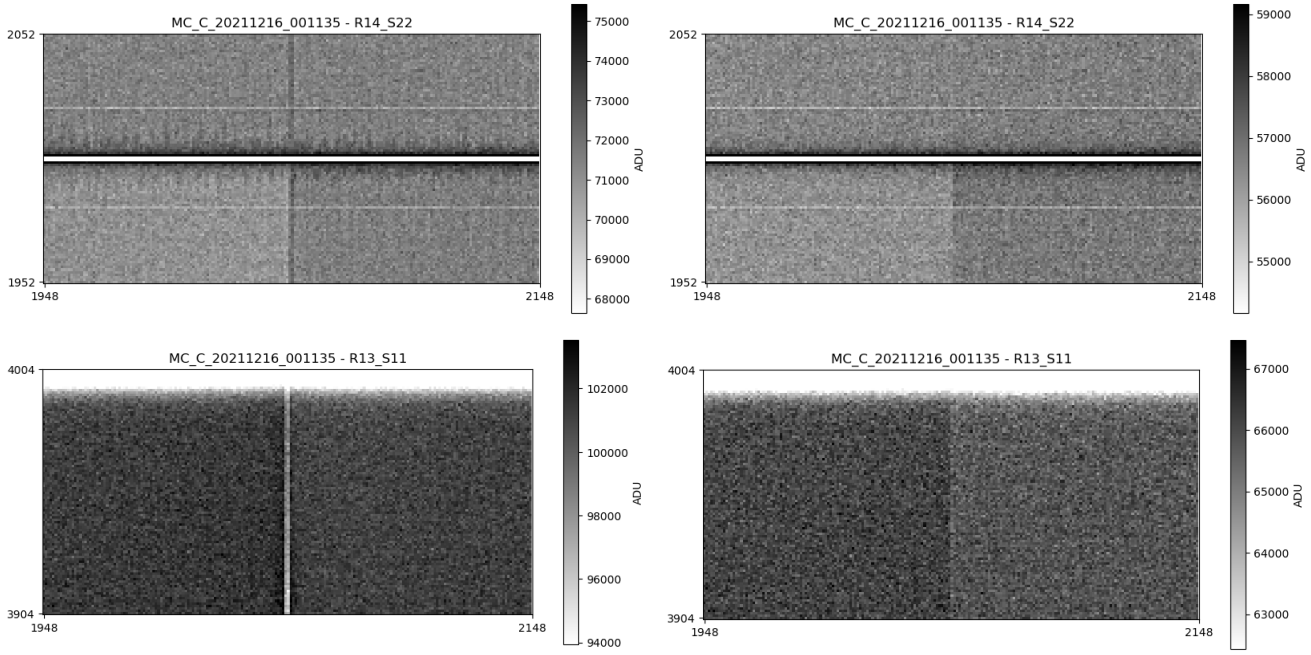

Figure 11. Two different types of tearing. (Top left) Classical tearing seen around the midline break. (Top right) Classical tearing mitigated with the Run 5 set of voltages (see Table 2). (Bottom left) Divisadero tearing seen between amplifier boundaries (Bottom right) tearing mitigated with the Run 5 voltage boundaries.

transfer.

5.7 Temperature dependence & feedback

Temperature changes with time in readout electronics induces changes in characteristics of components in general, resulting in gain variation. In the LSST vacuum cryostat, the REBs are thermally coupled to the cold plate, which is cooled to and maintained at about −40 C by the cold refrigeration system. Thanks to this active cooling, the cold plate temperature is very steady. The temperature variations are less than one degree C on time scales of hours. But this small variation still induces gain changes.

In order to investigate these changes, we acquired a number of flat images as well as photodiode measurements of the light source output. In this analysis, we used Run 13535 which collected 1110 flat images of 15 s integration time with a target level of 15,000 ADU over 24 hours. The measured temperature variations of thermistors in the REBs is about 1 C. After applying basic instrumental signature removal to the flat images, we measured the mean flat signal level in each image. The mean signal is divided by the integral of photodiode signal to make a measure of relative gain. We looked for correlation with other temperature measurements and found that the two temperature sensors on the REB board that are closest to the ASPIC (designated TEMP6 and TEMP10), are correlated well with the relative gain. We used `scipy.stats.linregress` to fit temperature and relative gain data. Figure 15 displays the temperature coefficients of gain for all the amplifiers. We will implement a gain correction based on the temperature measurements.

6. DISCUSSION: REMAINING FOCAL PLANE CCD ISSUES

6.1 Bias instability

Figure 16 shows an example of bias instability. In a bias image for a few amplifiers in E2V sensors we observed a few cases for which regular bias subtraction schemes leave a residual image shape around the corner with the readout node. We attempted to remove the bias 'shape' by using subtracting the serial overscan medianed row by row as well as by incorporating parallel overscan subtraction. The figure shows the residual after we apply both

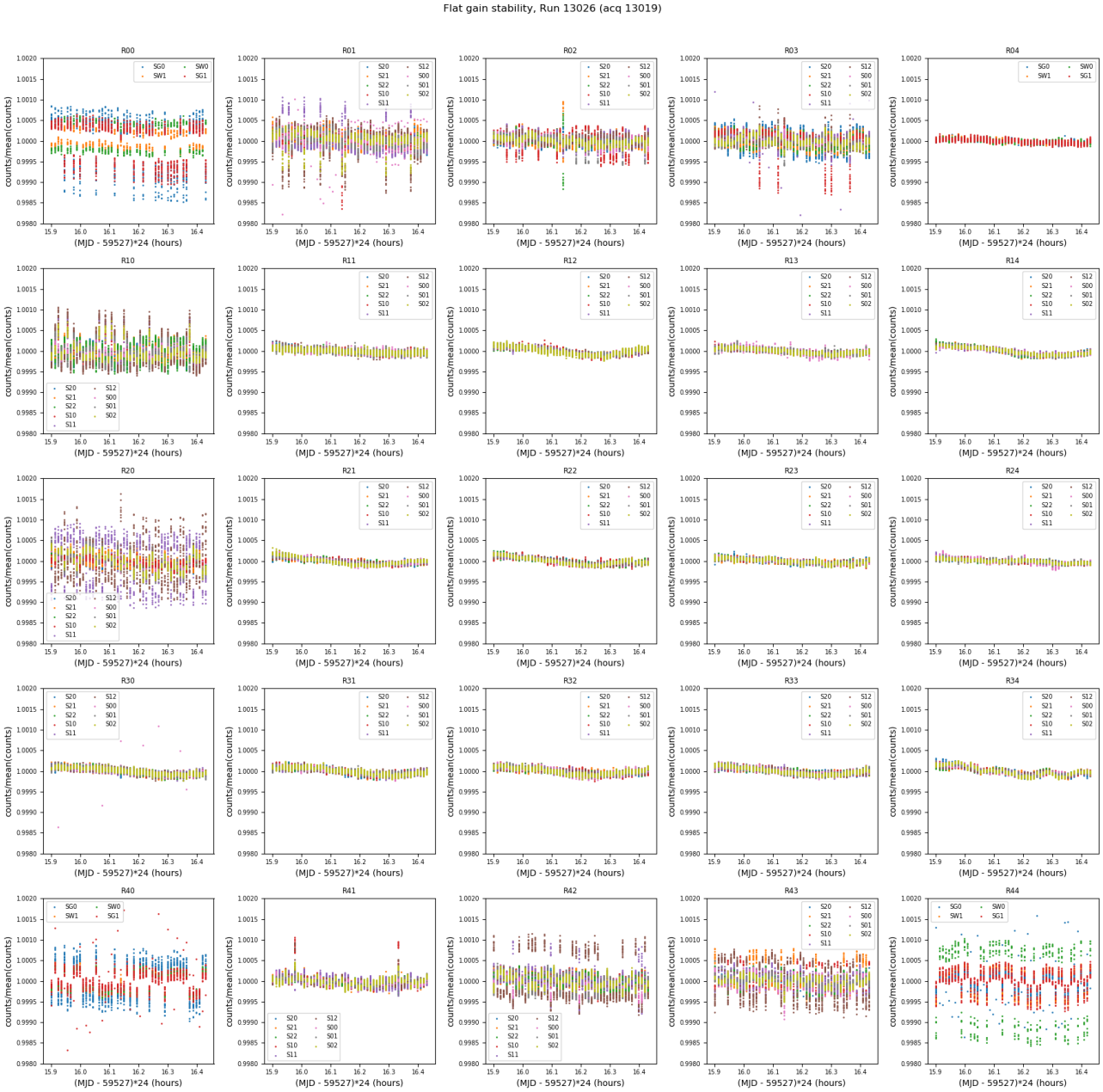

Figure 12. Relative gain stability derived from a series of flat images. Each panel corresponds to one raft. The 0.2% scatter observed in ITL-based rafts (see their locations in Fig. 3) is largely mitigated by changing ODV to 26.9 V. We did not further explore a higher OD since we were satisfied with the level of the gain variation. The plot shows the result before optimization (ODV=25.0V).

serial and parallel overscan subtraction. Amps 12 and 14 show residuals even with the overscan subtractions applied.

We quantify the effect by evaluating the mean signal at 200×200 pixels at the readout corner (where the greatest residual signal exists). We repeat this analysis for biases we collected and display in Figure 16. The level is on the order of 1 ADU; however, it changes over time, which makes it more difficult to deal with.

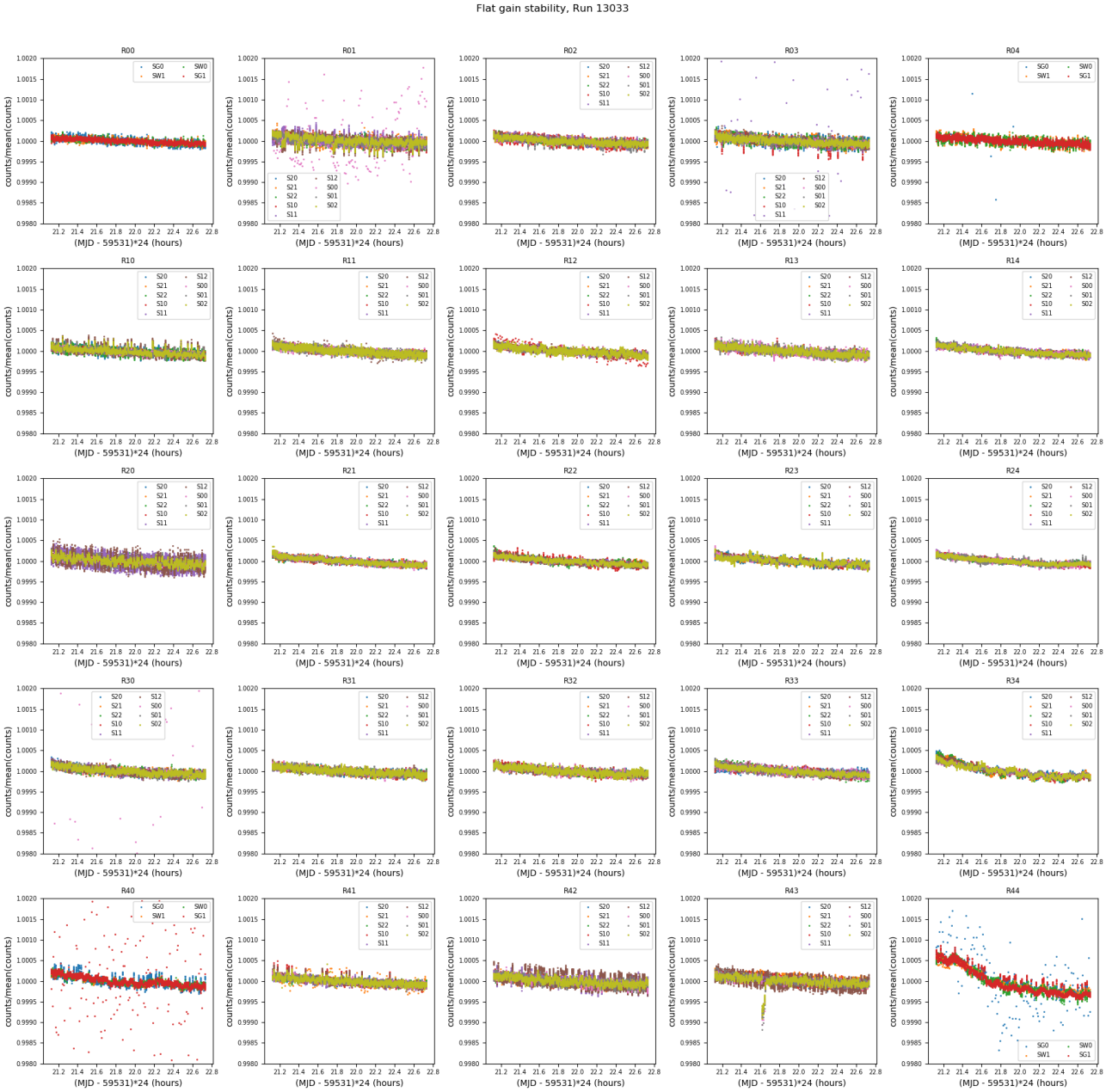

Figure 13. Same as Figure 12 but for the run after optimization (ODV=26.9)

We evaluated changes to how we operate E2V CCDs to mitigate this effect via several potential adjustments to the baseline configuration:

- Increasing the number of flushes of the serial register before starting readout from 10 to 100 (data-taking run 13051);
- No clear between exposures (13055);
- Making the rate of toggling CL faster during integration. (13056);

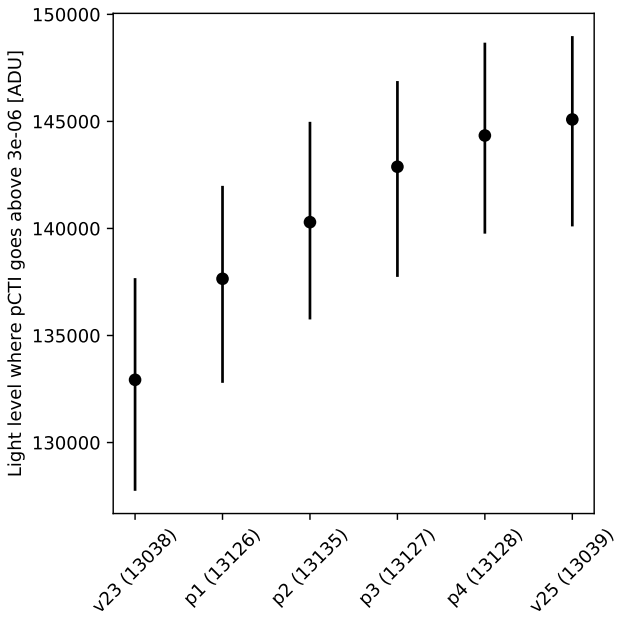

Figure 14. Parallel CTI (pCTI) turnoff as a function of different parallel timings. pCTI turnoff is defined as the light level above which the pCTI increases above 3×10^{-6}. The unit elements of parallel transfer (TimeP) of v23 and v25 are 5000 ns and 10000 ns, respectively. These pCTI values are linearly interpolated to investigate the full well change with respect to the parallel timing. The symbols are placed at the median (50th percentile) and error bars indicate 1 σ equivalent (32nd and 68th percentiles).

- Running serial register flush during integration, which usually generates serial register glow (13062);
- Running a serial register flushes slowly between exposures (13070);
- Running serial register flushes in a regular way between exposures (13069);
- Running pixel reads (ReadPixel) between exposures (13071);
- Running Deep Clear (Clear CCD once (fast) + 2 Deep Line Flushes) (13074);

The regular Clear does parallel transfers by the number of rows, then serial transfers by the number of columns, and finally inverts parallel clocks for 3 ms.

As the figure shows, running ReadPixel between exposures greatly suppresses the bias instability. Some amplifiers behave differently than others (Amp 5 of R33/S02 is the obvious case). However, running ReadPixel generates unnecessary heat since it runs the readout electronics chain continuously. An alternative approach is being investigated.

6.2 Persistence

In E2V sensors, we observed persistence in the exposures subsequent to exposures in which an excessive amount of charge was accumulated. Figure 17 shows an example. In columns where the charges were accumulated we also observed trailing persistence from the point of accumulation. The persistence started to be evident at light levels of $\sim$ 100 kADU. The level of persistence is 6 ADU on average, but varies from sensor to sensor. The decay constant is about 35 s, long enough to affect a few sucessive exposures.

We believe that the persistence is caused by the interface trap between Si and SiO_2 layers as charges are accumulated. In order to eliminate persistence we need to realize either a "pinned" condition or "blooming full well".[23] The pinned condition can be realized if we bias the output gate negatively enough. As the gate voltage

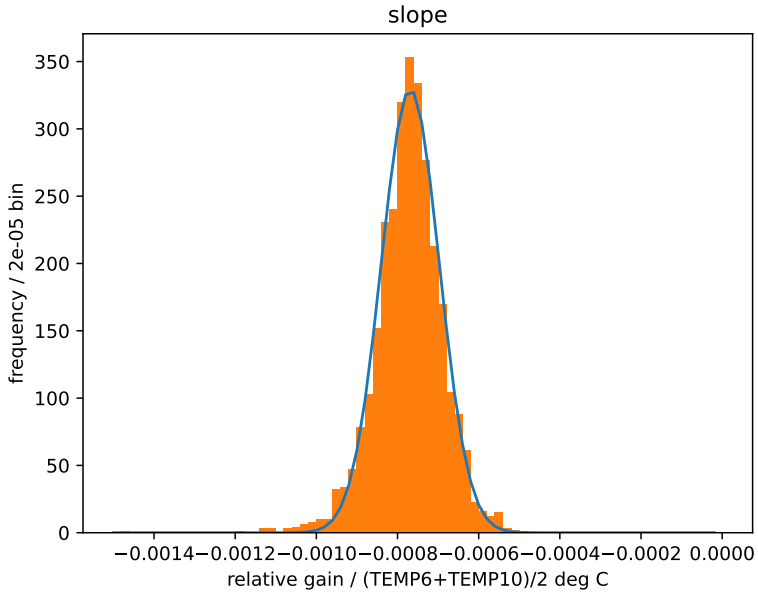

Figure 15. Gain-temperature coefficients derived from flat stability runs. TEMP6 and TEMP10 are the temperature sensors closest to the ASPICs on the REBs. The average their readings is used as a proxy for the temperature inducing the gain change.

is lowered, when the surface potential reaches the reference voltage, the condition is met. In this condition, holes from the channel stop region are attracted and collected at the Si-SiO_2 interface, which makes a layer of holes at the surface. Any excessive charges are then recombined with the holes at the surface and would not produce a persistence image. This would be done by changing the parallel low voltage. The reason why we do not choose to realize the pinned condition is that a safety concern is raised by the vendor. If we adopt a lower parallel low voltage, increased current flow, $\sim 10\,\mu$A for 3 CCDs, going across the sensor as the sensor accumulates excessive charge is observed. This excessive current flow (larger than $20\,\mu$A per a CCD) could possibly result in a breakdown in the sensor.

Another possibility is making "blooming full well" lower than "surface full well". In this condition charges bloom along the columns before charges get trapped by the interface layer. This requires lowering the barrier phases (PclkHigh) that confine accumulated charges. This will also likely mitigate the persistence issue; however, this also reduces the full well level. The other condition, "surface full well" is the condition that exposes the surface layer to charges. In the surface full well condition, full well is increased above the blooming full well. However, this condition above surface full well but below blooming full well does not have the same linearity as at lower signal since charges above the surface full well will recombine with the holes at the surface layer. Questions about whether the effect can be accounted for with a linearity correction, including whether it is repeatable, need to be investigated and the actual merit and demerits evaluated.

Tweaking parallel voltages also couples with tearing mitigation. Fundamentally, both persistence and tearing could be consequences of the same or similar physical mechanism – non-uniform hole distribution. We are currently assessing the impact of lowering the parallel voltage swing.

There is no noticeable persistence in ITL sensors.

7. CONCLUSIONS

We conducted extensive electro-optical testing of the LSST Camera at the level of the focal plane alone, and for the integrated full camera level. Using automated analysis tools, we characterized sensor performance in terms of

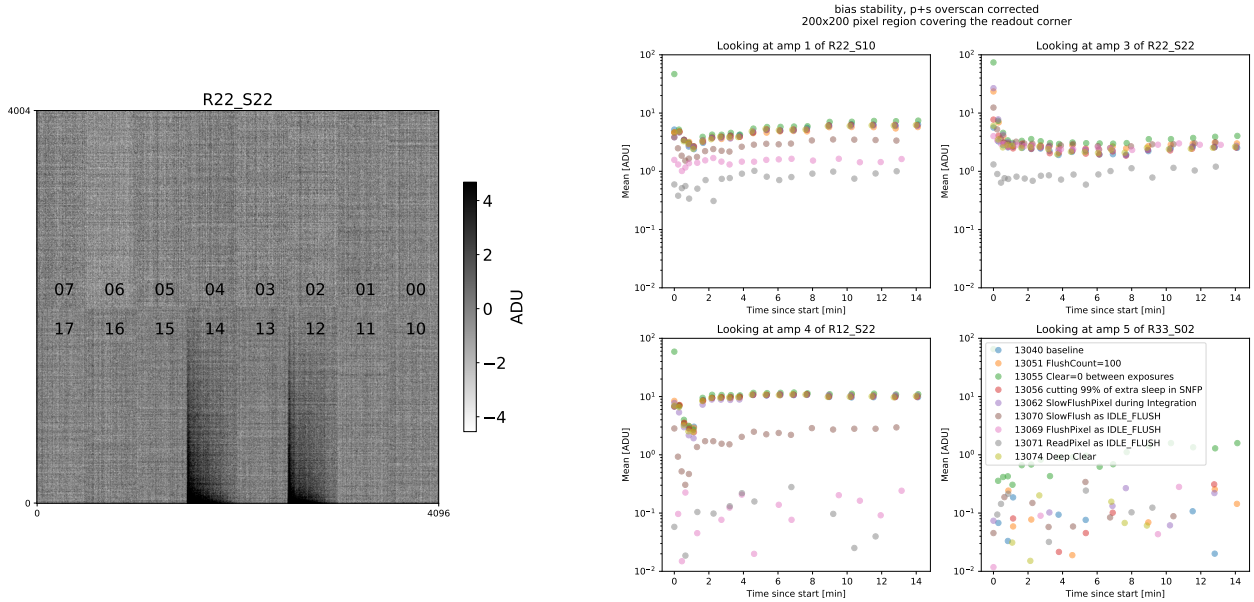

Figure 16. (left) The first bias image for a data-taking run (13040) with the rowcol overscan subtraction, after the system was idle for some time. R22/S22 is displayed. 4×4 binning is applied. In Segments 12 and 14, a $\sim$6 ADU level residual on the left bottom corner (where the readout nodes are located), while the other segments do not exhibit such residuals. For clarity, we inverted color, the darker is brighter. (right) Each strategy applied (see legend) had some impact on reducing the residual signals around the corners of the readout amplifiers of segments 12 (amp 3) and 14 (amp 5).

read noise, dark current, linearity, full well, serial and parallel CTI. The performance for these quantities meets the requirements for the LSST Camera.

We further explored non-idealities of the sensor. Pixel correlation called Dipoles was removed by making two of the parallel phases high during the integration. The read noise is improved by changing RampTime of Dual Slope Integration. Tearing is greatly suppressed by significant changes in voltages and clocking. Long-range serial correlations were mitigated by changing RD. Gain jumps were fixed by increasing OD by 1.9 V. Full well capacity is improved by parallel timing changes. The dependence of gain on the temperature of the readout electronics is characterized.

Mitigations for some additional sensor non-idealities are still under study. Bias stability is improved by running ReadPixel between exposures. However, an alternative approach is being investigated to reduce the thermal load. Persistence is present in E2V devices. We are currently investigating mitigations.

ACKNOWLEDGMENTS

This material is based upon work supported in part by the National Science Foundation through Cooperative Agreement AST-1258333 and Cooperative Support Agreement AST-1202910 managed by the Association of Universities for Research in Astronomy (AURA), and the Department of Energy under Contract No. DE-AC02-76SF00515 with the SLAC National Accelerator Laboratory managed by Stanford University. Additional Rubin Observatory funding comes from private donations, grants to universities, and in-kind support from LSST-DA Institutional Members.

REFERENCES

[1] Ivezić, Ž., Kahn, S. M., Tyson, J. A., and et al., "LSST: From Science Drivers to Reference Design and Anticipated Data Products," **873**, 111 (Mar. 2019). DOI: https://doi.org/10.3847/1538-4357/ab042c.

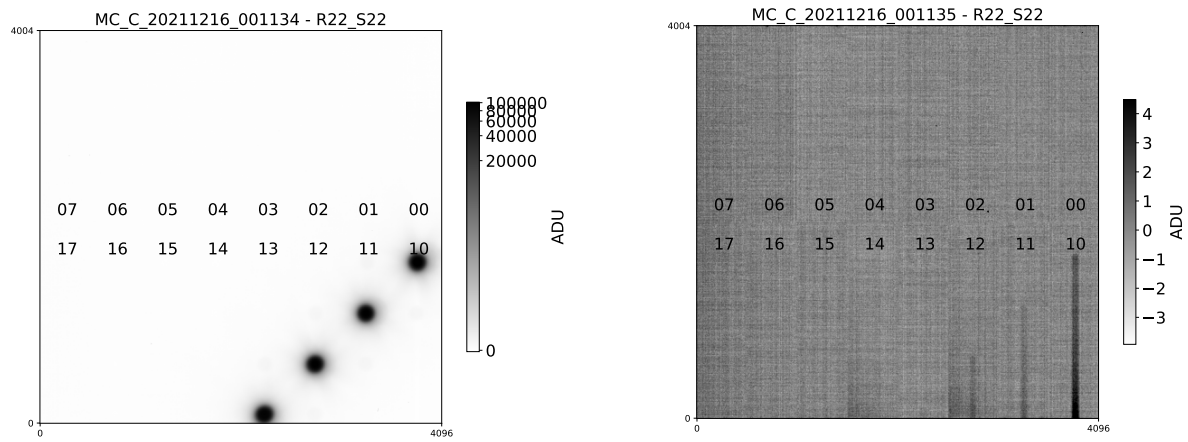

Figure 17. Persistence is seen in the bias image taken immediately after a bright spot acquisition. (left) A bright spot image that induces persistence (log stretch with Min Max interval) (right) A subsequent image showing persistence from the previous exposure (linear stretch with Zscale interval)

[2] O'Connor, P., Antilogus, P., Doherty, P., Haupt, J., Herrmann, S., Huffer, M., Juramy-Giles, C., Kuczewski, J., Russo, S., Stubbs, C., and Van Berg, R., "Integrated system tests of the LSST raft tower modules," in [*High Energy, Optical, and Infrared Detectors for Astronomy VII*], Holland, A. D. and Beletic, J., eds., *Society of Photo-Optical Instrumentation Engineers (SPIE) Conference Series* **9915**, 99150X (July 2016). DOI: https://doi.org/10.1117/12.2232729.

[3] Riot, V. J., Arndt, K., Claver, C., Doherty, P. E., Gilmore, D. K., Hascall, P. A., Herrmann, S., Kotov, I., O'Connor, P., Sebag, J., Stubbs, C. W., and Warner, M., "The guider and wavefront curvature sensor subsystem for the Large Synoptic Survey Telescope," in [*Ground-based and Airborne Instrumentation for Astronomy V*], Ramsay, S. K., McLean, I. S., and Takami, H., eds., *Society of Photo-Optical Instrumentation Engineers (SPIE) Conference Series* **9147**, 914774 (Aug. 2014). DOI: https://doi.org/10.1117/12.2056605.

[4] Ivezic, Z. et al., "Lsst science requirements document," (2013). https://ls.st/LPM-17.

[5] Kotov, I. V., Haupt, J., O'Connor, P., Smith, T., Takacs, P., Neal, H., and Chiang, J., "Characterization and acceptance testing of fully depleted thick CCDs for the large synoptic survey telescope," in [*High Energy, Optical, and Infrared Detectors for Astronomy VII*], Holland, A. D. and Beletic, J., eds., *Society of Photo-Optical Instrumentation Engineers (SPIE) Conference Series* **9915**, 99150V (July 2016). DOI: https://doi.org/10.1117/12.2231925.

[6] Doherty, P. E., Antilogus, P., Astier, P., Chiang, J., Gilmore, D. K., Guyonnet, A., Huang, D., Kelly, H., Kotov, I., Kubanek, P., Nomerotski, A., O'Connor, P., Rasmussen, A., Riot, V. J., Stubbs, C. W., Takacs, P., Tyson, J. A., and Vetter, K., "Electro-optical testing of fully depleted CCD image sensors for the Large Synoptic Survey Telescope camera," in [*High Energy, Optical, and Infrared Detectors for Astronomy VI*], Holland, A. D. and Beletic, J., eds., *Society of Photo-Optical Instrumentation Engineers (SPIE) Conference Series* **9154**, 915418 (July 2014). DOI: https://doi.org/10.1117/12.2056733.

[7] Snyder, A., Gilmore, K., and Roodman, A., "Optimization of CCD operating voltages for the LSST camera," in [*High Energy, Optical, and Infrared Detectors for Astronomy VIII*], Holland, A. D. and Beletic, J., eds., *Society of Photo-Optical Instrumentation Engineers (SPIE) Conference Series* **10709**, 107092B (July 2018). DOI: https://doi.org/10.1117/12.2313875.

[8] Snyder, A., Longley, E., Lage, C., Digel, S., Neal, H., Utsumi, Y., and Roodman, A., "Characterization and correction of serial deferred charge in LSST camera ITL CCDs," *Journal of Astronomical Telescopes, Instruments, and Systems* **7**, 048002 (Oct. 2021). DOI: https://doi.org/10.1117/1.JATIS.7.4.048002.

[9] Bradshaw, A. K., Lage, C., and Tyson, J. A., "Characterization of LSST CCDs using realistic images, before first light," in [*High Energy, Optical, and Infrared Detectors for Astronomy VIII*], Holland, A. D. and Beletic, J., eds., *Society of Photo-Optical Instrumentation Engineers (SPIE) Conference Series* **10709**, 107091L (July 2018). DOI: https://doi.org/10.1117/12.2314276.

[10] Lage, C., "Physical and electrical analysis of LSST sensors," *arXiv e-prints* , arXiv:1911.09577 (Nov. 2019). DOI: https://doi.org/10.48550/arXiv.1911.09577.

[11] Park, H., Karpov, S., Nomerotski, A., and Tsybychev, D., "Tree rings in Large Synoptic Survey Telescope production sensors: its dependence on radius, wavelength, and back bias voltage," *Journal of Astronomical Telescopes, Instruments, and Systems* **6**, 011005 (Jan. 2020). DOI: https://doi.org/10.1117/1.JATIS.6.1.011005.

[12] Juramy, C., Antilogus, P. E., Guillou, L. L., and Sepulveda, E., "Tearing and related field distortions in deep-depletion charge-coupled devices," *Journal of Astronomical Telescopes, Instruments, and Systems* **5**(4), 041505 (2019). https://doi.org/10.1117/1.JATIS.5.4.041505.

[13] Esteves, J. H., Utsumi, Y., Snyder, A., Schutt, T., Broughton, A., Trbalic, B., Mau, S., Rasmussen, A., Plazas Malagón, A. A., Bradshaw, A., Marshall, S., Digel, S., Chiang, J., Rykoff, E., Waters, C., Soares-Santos, M., and Roodman, A., "Photometry, Centroid and Point-spread Function Measurements in the LSST Camera Focal Plane Using Artificial Stars," *Publications of the Astronomical Society of the Pacific* **135**, 115003 (Nov. 2023). DOI: https://doi.org/10.1088/1538-3873/ad0a73.

[14] Broughton, A., Utsumi, Y., Plazas Malagón, A., Waters, C., Lage, C., Snyder, A., Rasmussen, A., Marshall, S., Chiang, J., Murgia, S., and Roodman, A., "Mitigation of the Brighter-Fatter Effect in the LSST Camera," *arXiv e-prints* , arXiv:2312.03115 (Dec. 2023). DOI: https://doi.org/10.48550/arXiv.2312.03115.

[15] Roodman, A., Bogart, J. R., Bond, T., Borgland, A. W., Chiang, J., Digel, S. W., Dubois, R., Focke, W. B., Glanzman, T., Gilmore, K., Hascall, D., Hascall, P., Herrmann, S., Johnson, A. S., Kelly, H. M., Lange, T., Lopez, M., Marshall, S., Neal, H., Newbry, S., Nordby, M., Rasmussen, A., Reil, K., Rosenberg, E., Russo, S., Saxton, O., Snyder, A., Tether, S., Turri, M., Utsumi, Y., O'Connor, P., Nomerotski, A., Rumore, M., Haupt, J., Takacs, P., Barrau, A., Combet, C., Dargaud, G., Eraud, L., Marton, M., Migliore, M., Perbet, E., Ricol, J. S., Vescovi, C., Doherty, P., Baumann, B., Winters, S., Wolfe, J., Antilogus, P., and Juramy, C., "Integration and verification testing of the LSST camera," in [*Modeling, Systems Engineering, and Project Management for Astronomy VIII*], Angeli, G. Z. and Dierickx, P., eds., *Society of Photo-Optical Instrumentation Engineers (SPIE) Conference Series* **10705**, 107050D (July 2018). DOI: https://doi.org/10.1117/12.2314017.

[16] Bond, T., Roodman, A., Reil, K., Lange, T., Nordby, M., Newbry, S., Lopez, M., Bowdish, B., Lee, V., Hascall, D., Munoz, J., Marshall, S., Rasmussen, A., Digel, S., Utsumi, Y., and Snyder, A., "LSST camera - integration and test subsystem: planning and status," in [*Modeling, Systems Engineering, and Project Management for Astronomy VIII*], Angeli, G. Z. and Dierickx, P., eds., *Society of Photo-Optical Instrumentation Engineers (SPIE) Conference Series* **10705**, 107050E (July 2018). DOI: https://doi.org/10.1117/12.2314244.

[17] Snyder, A., Barrau, A., Bradshaw, A., Bowdish, B., Chiang, J., Combet, C., Digel, S., Dubois, R., Eraud, L., Juramy, C., Lage, C., Lange, T., Migliore, M., Nomerotski, A., O'Connor, P., Park, H. Y., Rasmussen, A., Reil, K., Roodman, A., Shestakov, A., Utsumi, Y., and Wood, D., "Laboratory measurements of instrumental signatures of the LSST camera focal plane," in [*X-Ray, Optical, and Infrared Detectors for Astronomy IX*], Holland, A. D. and Beletic, J., eds., *Society of Photo-Optical Instrumentation Engineers (SPIE) Conference Series* **11454**, 1145439 (Dec. 2020). DOI: https://doi.org/10.1117/12.2562915.

[18] O'Connor, P., Kotov, I., Takacs, P. Z., Frank, J. S., Plate, S., Van Berg, R., Newcomer, M., Antilogus, P., Lebbolo, H., Tocut, V., Juramy, C., Doherty, P., and Felt, N., "Development of the LSST raft tower modules," in [*High Energy, Optical, and Infrared Detectors for Astronomy V*], Holland, A. D. and Beletic, J. W., eds., *Society of Photo-Optical Instrumentation Engineers (SPIE) Conference Series* **8453**, 84530L (July 2012). DOI: https://doi.org/10.1117/12.926645.

[19] Juramy, C., Antilogus, P., Bailly, P., Baumont, S., Dhellot, M., El Berni, M., Jeglot, J., Lebbolo, H., Martin, D., Qureshi, A., Russo, S., Terront, D., Tocut, V., and Vallerand, P., "Driving a CCD with two ASICs: CABAC and ASPIC," in [*High Energy, Optical, and Infrared Detectors for Astronomy VI*], Holland, A. D. and Beletic, J., eds., *Society of Photo-Optical Instrumentation Engineers (SPIE) Conference Series* **9154**, 91541P (July 2014). DOI: https://doi.org/10.1117/12.2055175.

[20] Antilogus, P., Bailly, P., Barrillon, P., Dhellot, M., El berni, A., Jeglot, J., Juramy-Gilles, C., Lebbolo, H., Martin, D., Moniez, M., and Vallerand, P., "ASPIC and CABAC: two ASICs to readout and pilot CCD," *Journal of Instrumentation* **12**, C03017 (Mar. 2017). DOI: https://doi.org/10.1088/1748-0221/12/03/C03017.

[21] Newbry, S., Lange, T., Roodman, A., Reil, K., Bond, T., Rasmussen, A., Bowdish, B., Snyder, A., Rosenberg, E., and Lee, V., "LSST camera bench for optical testing: design, assembly, and preliminary testing," in [*Ground-based and Airborne Instrumentation for Astronomy VII*], Evans, C. J., Simard, L., and Takami, H., eds., *Society of Photo-Optical Instrumentation Engineers (SPIE) Conference Series* **10702**, 1070258 (July 2018). DOI: https://doi.org/10.1117/12.2314269.

[22] Bosch, J., AlSayyad, Y., Armstrong, R., Bellm, E., Chiang, H.-F., Eggl, S., Findeisen, K., Fisher-Levine, M., Guy, L. P., Guyonnet, A., Ivezić, Ž., Jenness, T., Kovács, G., Krughoff, K. S., Lupton, R. H., Lust, N. B., MacArthur, L. A., Meyers, J., Moolekamp, F., Morrison, C. B., Morton, T. D., O'Mullane, W., Parejko, J. K., Plazas, A. A., Price, P. A., Rawls, M. L., Reed, S. L., Schellart, P., Slater, C. T., Sullivan, I., Swinbank, J. D., Taranu, D., Waters, C. Z., and Wood-Vasey, W. M., "An Overview of the LSST Image Processing Pipelines," in [*Astronomical Data Analysis Software and Systems XXVII*], Teuben, P. J., Pound, M. W., Thomas, B. A., and Warner, E. M., eds., *Astronomical Society of the Pacific Conference Series* **523**, 521 (Oct. 2019). DOI: https://doi.org/10.48550/arXiv.1812.03248.

[23] Janesick, J., [*Scientific Charge-coupled Devices*], SPIE Press (2001). DOI: https://doi.org/10.1117/3.374903.